Quantum Delocalization Enables Water Dissociation on Ru(0001)

Quantum Delocalization Enables Water Dissociation on Ru(0001)

Yu Cao,[1,2,*] Jiantao Wang,[1,2,*] Mingfeng Liu,[1] Yan Liu,[1,2] Hui Ma,[1]
Cesare Franchini,[3,4] Yan Sun,[1] Georg Kresse,[3] Xing-Qiu Chen,[1,†] and Peitao Liu[1,‡]

[1]*Shenyang National Laboratory for Materials Science, Institute of Metal Research, Chinese Academy of Sciences, 110016 Shenyang, China*
[2]*School of Materials Science and Engineering, University of Science and Technology of China, 110016 Shenyang, China*
[3]*University of Vienna, Faculty of Physics and Center for Computational Materials Science, Kolingasse 14-16, A-1090 Vienna, Austria*
[4]*Dipartimento di Fisica e Astronomia, Università di Bologna, 40127 Bologna, Italy*

We revisit the long-standing question of whether water molecules dissociate on the Ru(0001) surface through nanosecond-scale path-integral molecular dynamics simulations on a sizable supercell. This is made possible through the development of an efficient and reliable machine-learning potential with near first-principles accuracy, overcoming the limitations of previous *ab initio* studies. We show that the quantum delocalization associated with nuclear quantum effects enables rapid and frequent proton transfers between water molecules, thereby facilitating the water dissociation on Ru(0001). This work provides the direct theoretical evidence of water dissociation on Ru(0001), resolving the enduring issue in surface sciences and offering crucial atomistic insights into water-metal interfaces.

The interaction of water with solid surfaces plays an important role in various scientific and technical fields, including ice nucleation, catalysis, lubrication, and corrosion [1–3]. The subtle interplay between the water-solid interface and water-water hydrogen bonding interactions results in complex structural motifs of water on surfaces, prompting extensive experimental and theoretical investigations [4–11]. Among these studies, the water overlayer on the Ru(0001) surface is notably one of the most debated systems.

Initially, it was commonly believed that the first-layer water molecules on Ru(0001) would arrange themselves into a bulk-ice-like bilayer [12–15]. However, this notion was challenged by the low-energy electron diffraction (LEED) analysis by Held and Menzel [16, 17], which revealed nearly coplanar O atoms with a vertical distance of just 0.14 Å [17], significantly smaller than that of the ice-like bilayer. Moreover, density functional theory (DFT) calculations employing commonly used generalized gradient approximation functionals predicted that the ice-like bilayer did not even wet the surface [18]. To resolve this discrepancy, Feibelman proposed a partially dissociated overlayer model [18], which not only reproduced the experimental observation of almost coplanar O atoms, but also demonstrated superior energetic stability compared to the H-up or H-down bilayers as well as the sublimation energy of ice-Ih [18].

Feibelman's study [18] raised an even today debated question—whether the water molecules within the overlayer dissociate on Ru(0001)? Experimental evidence from sum-frequency generation vibrational spectroscopy [19] and reflection adsorption infrared spectroscopy [20, 21] indicated that the water remained intact on Ru(0001) at low temperatures. However, temperature programmed desorption measurements observed residual atomic hydrogen on the surface after water desorption, implying the dissociative adsorption [22]. The situation became even more puzzling by conflicting x-ray photoelectron spectroscopy (XPS) studies [23–26]. Andersson *et al.* attributed the flat water-hydroxyl overlayer observed by LEED to electron beam damage and claimed that the water dissociation was a thermal or electron stimulated process [23], which was later supported by two independent XPS studies [24, 25]. In contrast, Weissenrieder *et al.* provided experimental XPS evidence for a partially dissociated water bilayer on Ru(0001) at temperatures as low as 105 K using beam-damage-free low photon flux [26]. Besides XPS, scanning tunneling microscopy (STM) also unveiled perplexing results. Tatarkhanov *et al.* [27] and Maier *et al.* [28, 29] demonstrated through STM that at temperatures below 130 K, the deposited water remained intact and tended to form stripes of hexagons. However, a more recent STM investigation by Schilling and Behm [30] indicated that partial water dissociation could possibly occur already during slow adsorption at 120 K.

The conflicting experimental results also stimulated extensive DFT calculations [32–40]. Consistent with Feibelman's predictions, Michaelides *et al.* [32, 33] confirmed that the partially dissociated overlayer was thermodynamically more stable than any identified water bilayers. Nevertheless, the predicted dissociation energy barrier was higher than the mean adsorption energy of the water bilayers [34, 35], indicating the favorable desorption of water over dissociation. To address the problems associated with the coplanar overlayer observed by LEED and the underestimated work function change upon adsorption for the half-dissociated model, a metastable structure with mixed intact H-up and H-down molecules [35], and an extended chains model containing chains of flat-lying and chains of H-down molecules [21, 38] were suggested.

Despite comprehensive DFT studies, the ground-state structure of water overlayers on Ru(0001) remains inconclusive due to the vast configuration space originating from the complex hydrogen bonding networks and water-metal interactions. Additionally, whether the water overlayers dissociate on Ru(0001) remains elusive, given the high predicted dissociation energy barrier (0.5 eV [32] and 0.62 eV [35]). Aiming to address these questions, we developed an accurate, efficient, and robust machine-learning potential, which not only facilitates the accurate exploration of the potential energy surface (PES) landscape for water adsorption on Ru(0001) at various

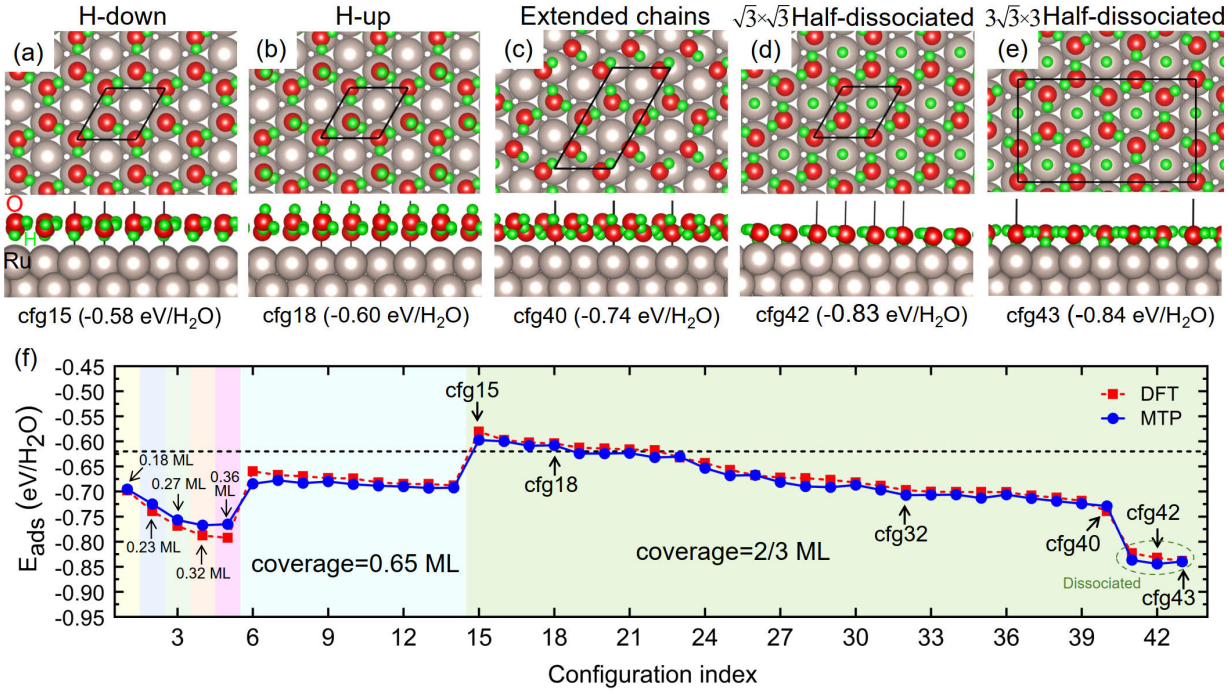

Figure 1. Top and side views of (a) H-down, (b) H-up, (c) extended chains, (d) $\sqrt{3}\times\sqrt{3}$ half-dissociated [26], and (e) $3\sqrt{3}\times 3$ half-dissociated [18] water overlayer models. The black lines indicate the unit cell. (f) The DFT and MTP predicted adsorption energies of H_2O on Ru(0001) for the 43 considered configurations at various coverages (see Supplemental Material Fig. S2 [31]). The dashed line denotes the sublimation energy of ice-Ih.

coverages, but also allows for long-time scale path-integral molecular dynamics (PIMD) simulations. Our work provides direct and compelling evidence of water dissociation from an intact overlayer on Ru(0001), which is driven by nuclear quantum effects (NQEs).

We begin by constructing and validating our moment tensor potential (MTP) [41]. Following the scheme outlined in Refs. [42, 43], the training dataset was initially acquired through an on-the-fly active learning procedure [44, 45] implemented in the Vienna *ab initio* simulation package (VASP) [46, 47], and subsequently expanded iteratively using the active learning method implemented in the MLIP package [48]. First-principles calculations were performed using VASP [46, 47] employing the revised Perdew-Burke-Ernzerhof (RPBE) functional for its improved adsorption energetics [49]. Van der Waals (vdW) interactions were included using the D3 method of Grimme *et al.* [50] with zero damping. We found that RPBE+D3 yielded similar Ru-O and O-O vertical distances and relative water adsorption energies when compared to SCAN [51], PBE+D3 [50, 52], and optB88-vdW [53] functionals (Supplemental Material Table S1 and Fig. S1 [31]). The training dataset contained 6,813 structures including bulk ice-Ih, bulk Ru, and the clean Ru(0001) surface, as well as intact and dissociated water overlayers at various coverages up to 2/3 monolayer (ML) (Supplemental Material Table S2 [31]). To enhance the efficiency, the MTP was fitted with the optimized basis sets by refining the contraction process of moment tensors using our in-house code (IMR-MLP) [54]. The MTP was validated on a test dataset of 600 structures including bulk Ru, the clean Ru(0001) surface, intact and half-dissociated water overlayers at 2/3 ML (Supplemental Material Table S3 [31]). These test structures were randomly sampled from MD simulations. The MTP demonstrates a high accuracy, with validation root-mean-square errors of 1.02 meV/atom for energies and 59 meV/Å for forces (Supplemental Material Fig. S3 [31]). More computational details can be found in the Supplemental Material [31].

The developed MTP allows us to efficiently explore the PES of water overlayers at different coverages. As depicted in Fig. 1, for the considered 43 configurations including intact and dissociated water overlayers, the MTP accurately predicts their adsorption energies, showing remarkable agreement with DFT results. Particularly, we focus on the extensively studied 2/3 ML overlayers. It is evident that the H-down and H-up models exhibit comparable adsorption energies. However, both configurations would not wet the Ru(0001) surface, since their adsorption energies are lower than the sublimation energy of ice-Ih [see Fig. 1(f) and Supplemental Material Fig. S1(a) [31]]. The most stable intact overlayer identified at 2/3 ML is the extended chains model with a unit cell of $\sqrt{3}\times 2\sqrt{3}$, where the O atoms in the flat-lying chains are positioned atop Ru, whereas the O atoms in the H-down chains occupy the bridge sites [see Fig. 1(c)]. Note that this extended chains model is more stable by 0.04 eV/H_2O than the one

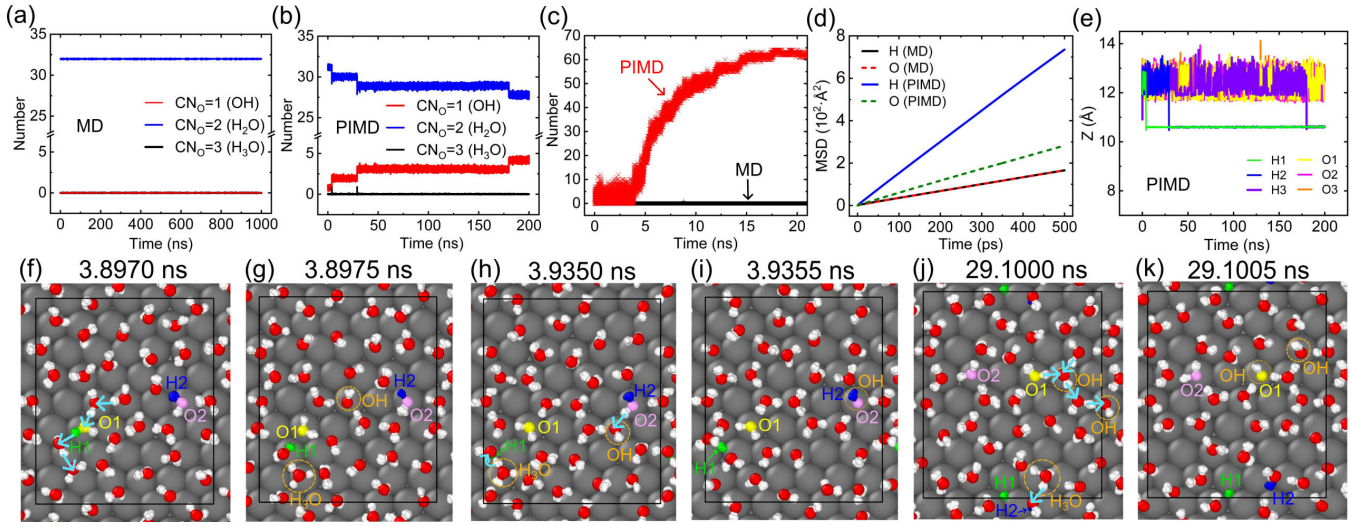

Figure 2. Time evolution of the number of OH (CN$_O$=1), H_2O (CN$_O$=2), and H_3O (CN$_O$=3) species in (a) classical MD and (b) PIMD simulations at 300 K. CN$_O$ represents the coordination number of the oxygen atom. (c) Time evolution of occurrences when either of the two hydrogen atoms in an H_2O molecule differs from the initial configuration at 0 ns. (d) Mean square displacements (MSD) of the O and H atoms. (e) Time evolution of the vertical distances of the H and O atoms [specified in (f)] in the PIMD simulation. (f)-(k) Snapshots from the PIMD trajectory. The tracked O and H atoms as well as the H_3O and OH species are highlighted. The cyan arrows depict the proton transfer process.

originally proposed by Hodgson *et al.* (i.e., cfg32) [21, 38], where all the O atoms are situated atop Ru. Generally, the dissociated overlayers (configurations 41-43 [18, 26]) exhibit coplanar O atoms and are more stable compared to the intact ones, consistent with previous calculations [18, 32–35].

We note that the overlayer configurations examined above are constrained to ordered phases with small unit cells, without fully incorporating the disorder effects. Experiments also face challenges in identifying hydrogen disorder due to its light mass [55]. To examine the disorder effects, we performed simulated annealing (SA) MD simulations on large supercells using the MTP and the LAMMPS code [56]. The most favorable intact (cfg40) and dissociative (cfg43) configurations were selected as initial structures. Two large supercells (i.e., $6\times3\sqrt{3}$ and $12\times6\sqrt{3}$) were employed to account for varying degrees of disorder. For each configuration, 90 independent SA runs were conducted, followed by structural relaxations. Interestingly, for the dissociative case, the lowest-energy configuration identified by SA exhibits only marginally higher stability (0.01 eV/H_2O energy gain) in comparison to the initial ordered phase (Supplemental Material Fig. S4 [31]). The slightly higher stability of cfg43 compared to cfg42 is also such a manifestation of disorder effects (Fig. 1). The disordered configurations accommodated within large supercells primarily exhibit disorder in hydrogen orientation, aimed at maximizing hydrogen bonding. However, for the intact case, we were unable to find a disordered configuration more favorable than the $\sqrt{3}\times2\sqrt{3}$ extended chains model within the 90 SA runs (Supplemental Material Fig. S4 [31]). This indicates a flat PES with numerous local minima, in agreement with Hodgson's findings [38]. In fact, the extended chains configuration is a model that already accounts for partial disorder in the O height and proton orientation [38]. For both the dissociative and intact cases, a supercell beyond the $6\times3\sqrt{3}$ unit cell almost shows no energy gain from disorder.

Having identified the most stable intact and dissociative overlayers, we now turn to tackling the enduring question of whether water overlayers dissociate on Ru(0001). First, we computed the dissociation energy barrier, yielding 0.53 eV for dissociating half of the water molecules, aligning with previous predictions [32, 35]. The energy barrier is found to be higher (>0.6 eV) for dissociating 1/8 of the water molecules (Supplemental Material Fig. S5 [31]). Based on a rough estimation from transition state theory [57], a dissociation energy barrier of this magnitude would necessitate a time scale exceeding microseconds, far beyond the accessible time-scale of MD simulations. Indeed, we did not observe the dissociation throughout a one-microsecond classical MD simulation [Fig. 2(a)]. Nevertheless, classical MD simulations do not take into account the NQEs, which have been shown to be significant in hydrogen-related systems [58–76]. In particular, Li *et al.* [63] showcased the pronounced NQEs for water overlayers on transition metal surfaces through *ab initio* PIMD simulations. Despite their high accuracy, *ab initio* methods face limitations concerning the accessible time and length scales, hindering the direct observation of water dissociations.

Thanks to our accurate and efficient machine-learning potential, we were able to perform PIMD simulations on large supercells for an extended timescale, while maintaining *ab initio* accuracy. In the PIMD simulations, 16 beads were employed to sample the imaginary time path-integral and the statistical analyses were derived by averaging these 16 beads.

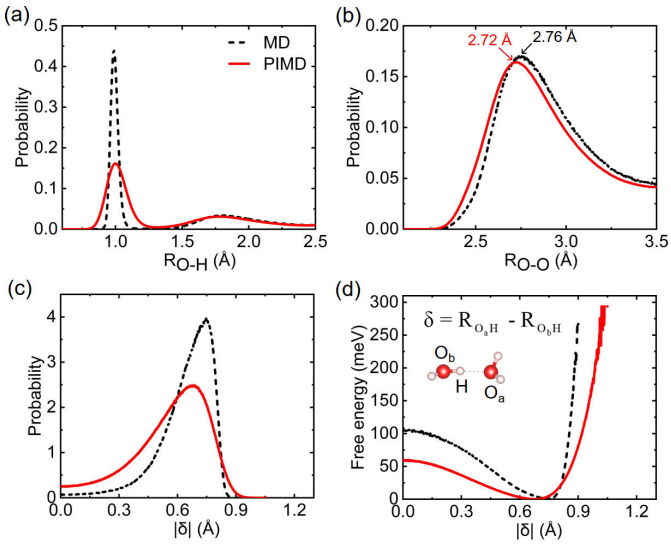

Figure 3. Probability distributions of (a) O-H and (b) O-O distances at 300 K. (c) Probability distribution of the proton transfer coordinate $|\delta| = |R_{O_aH} - R_{O_bH}|$, where R_{O_aH} denotes the distance between the O_a atom and the H atom [see the insert in (d)]. $|\delta|$=0 indicates that the shared H atom is exactly positioned between two O atoms. (d) Free energy profile for the protons along the intermolecular axes.

We employed a $6 \times 4\sqrt{3}$ supercell with 32 H_2O molecules based on the most stable intact overlayer configuration (i.e., extended chains model) as the initial structure. Throughout a 200-nanosecond PIMD simulation, three abrupt changes in the number of OH, H_2O, and H_3O species are observed [see Fig. 2(b)], indicating three instances of water dissociation. To corroborate our findings, we conducted additional independent PIMD and classical MD simulations. Water dissociation was consistently reproduced in all PIMD simulations but was absent in classical MD simulations within the considered timescale (Supplemental Material Fig. S7 [31]). Furthermore, PIMD simulations of D_2O adsorption on Ru(0001), conducted under identical computational settings as H_2O adsorption, revealed no dissociation. This result underscores the pronounced kinetic isotope effect and aligns with experimental observations [20]. Collectively, these results demonstrate that the NQEs facilitate the water dissociation on Ru(0001).

It is worth noting that such NQEs cannot be simply interpreted as the commonly assumed thermalization effect in classical MD simulations at elevated temperatures. This is because, even when the temperature is raised to 350 K, water dissociation does not occur within the same time frame in the classical MD simulation (Supplemental Material Fig. S7 [31]). Importantly, the NQEs result in a significant quantum delocalization of protons. This is evidenced by the broadened first peak in the probability distributions of O-H distances [Fig. 3(a)] as well as the enhanced probability distributions of protons within the central region of two adjacent oxygen atoms [Fig. 3(c)] observed in PIMD simulations, as compared to classical MD simulations. Moreover, the quantum delocalization of the shared protons between the two oxygen atoms slightly shortens the O-O distances [Fig. 3(b)], strengthening the hydrogen bonding. Our results agree well with the findings of Li *et al.* [63]. Furthermore, we computed the free energy profile for the protons along the intermolecular axes through $\Delta F(|\delta|) = -k_B T \ln[P(|\delta|)]$ following Ref. [63], where $P(|\delta|)$ represents the probability distribution of $|\delta| = |R_{O_aH} - R_{O_bH}|$ [see Fig. 3(c)] and k_B is the Boltzmann constant. One can see from Fig. 3(d) that the free energy barrier for proton transfer is just 59 meV in the PIMD simulation, a value notably lower than that observed in the classical MD simulation (~103 meV).

The small free energy barrier in PIMD simulations enables rapid and frequent proton transfers among water molecules [Figs. 2(c)-(d)]. Moreover, the emergence of water dissociation would enhance the rate of proton transfers [Fig. 2(c)]. Conversely, in classical MD simulations, the protons almost do not undergo transfers due to the large free energy barrier [Fig. 2(c)]. Specifically, in classical MD, the two H atoms and an O atom in an H_2O molecule consistently exhibit identical motions, whereas in PIMD, they follow distinct motion pathways due to the proton transfers [Fig. 2(d)]. Interestingly, we observe that while the dissociated H atoms diffuse most rapidly with a diffusion coefficient of 5.58×10^{-5} cm^2/s, the diffusion of H and O atoms within the water-hydroxyl overlayer is comparatively slower than within the intact overlayer (Supplemental Material Fig. S8 [31]). This might be related to the inhibited proton transfer by hydroxide ions [70].

To unveil the details of proton transfers and water dissociation, we analyzed the PIMD trajectory. Note that although PIMD does not provide a real-time picture of the trajectories, we still believe that the mechanisms we observe would prevail in a centroid molecular dynamics and that the observed mechanisms are highly relevant to water dissociation. Initially, ephemeral hydroxyls exist due to the quantum delocalization associated with the NQEs, as evidenced by the fluctuation between the number of hydroxyls and intact H_2O (Supplemental Material Fig. S9 [31]). At 3.8975 ns, the formation of an H_3O and OH pair commences due to the proton transfer [Figs. 2(f)-(g)], and the pair would typically last for ~38 ps (Supplemental Material Fig. S9 [31]). At 3.9355 ns, the first instance of water dissociation emerges. Interestingly, we observe that the dissociation does not directly originate from H_3O, but instead undergoes an indirect process. Specifically, one of the protons in H_3O is transferred to the neighboring H_2O, leading to the simultaneous dissociation of a hydrogen atom from the latter [Figs. 2(h)-(i)]. The dissociated H is observed to preferentially occupy the hollow fcc sites rather than the top sites on Ru(0001). This observation is consistent with our DFT calculations, when the dissociation fraction is low [Supplemental Material Fig. S5(l) [31]]. Moreover, we find that once dissociated, the dissociated H decreases its vertical height [Fig. 2(e)], diffuses on the surface, but is rarely involved in proton transfers. The existence of the dissociated hydroxyl increases the frequency of proton transfers [Fig. 2(c)]. At 29.1005 ns, the second occurrence

of water dissociation takes place, following a procedure akin to the first instance [Figs. 2(j)-(k) and Supplemental Material Fig. S10 [31]]. At 179.9685 ns, a third water molecule dissociates [Fig. 2(b)]. Notably, this third dissociation event does not involve the formation of H_3O (Supplemental Material Fig. S11 [31]). At this point, the system contains 29 intact water molecules, 3 hydroxyls, and 3 dissociated hydrogen atoms. Over extended time scales, a greater number of H_2O would likely dissociate. Note that within the simulated time frame, no water desorption was observed due to the higher energy barrier for desorption compared to dissociation (Supplemental Material Figs. S6 and S5 [31]). This aligns with experimental findings that H_2O dissociates prior to desorption [20]. However, the large computational cost of PIMD kept us from much longer simulations.

In summary, we have developed an efficient and robust machine-learning potential to accurately capture the intricate interactions between water overlayers and the Ru(0001) surface through active learning and basis sets optimization. This enables us to identify the most stable overlayers for both intact and dissociative adsorption and facilitate the execution of PIMD simulations with near first-principles accuracy on a time and length scale that is inaccessible through *ab initio* methods. This capability is crucial, as it allows us to directly observe water dissociation on Ru(0001) through a nanosecond-scale PIMD simulation, a remarkable achievement that is unattainable with previous *ab initio* studies. We clearly demonstrate that the water dissociation is driven by the quantum delocalization originating from NQEs. These are essential to facilitate rapid and frequent proton transfers. Furthermore, the formation of H and OH pairs appears to occur via long-range density fluctuations, with an H and OH pair forming quasi-instantly over a distance of up to 5 connected H_2O molecules. This is facilitated by a combination of the Grotthuss mechanism and quantum fluctuations. To our knowledge, such a long-range mechanism has not been observed before. Our study implies that quantum fluctuations can dramatically change the barriers to water dissociation, but also lead to new dissociation pathways. This has far-reaching implications not only for surface science, electrolysis and fuel cells, but also for biology, where water is ubiquitous. Clearly, our study suggests that quantum fluctuations must be taken into account whenever water dissociation occurs. The implications for the now so important field of hydrogen production are huge, as the barriers appear to be cut in half by quantum fluctuations.

This work is supported by the National Natural Science Foundation of China (Grants No. 52422112, No. 52188101, and No. 52201030), the Strategic Priority Research Program of the Chinese Academy of Sciences (XDA041040402), the Liaoning Province Science and Technology Major Project (2024JH1/11700032, 2023021207-JH26/103 and RC230958), the National Key R&D Program of China 2021YFB3501503, and the Special Projects of the Central Government in Guidance of Local Science and Technology Development (2024010859-JH6/1006).

Data availability—The data that support the findings of this article are openly available [77].

* These authors contribute equally to this work.
† xingqiu.chen@imr.ac.cn
‡ ptliu@imr.ac.cn

[1] Rentao Mu, Zhi-jian Zhao, Zdenek Dohnálek, and Jinlong Gong, "Structural motifs of water on metal oxide surfaces," Chem. Soc. Rev. **46**, 1785–1806 (2017).
[2] Daniel A. Knopf and Peter A. Alpert, "Atmospheric ice nucleation," Nature Reviews Physics **5**, 203–217 (2023).
[3] Sheng Meng and Enge Wang, *Water*, 1st ed. (Springer Singapore, 2023).
[4] A. Hodgson and S. Haq, "Water adsorption and the wetting of metal surfaces," Surface Science Reports **64**, 381–451 (2009).
[5] Javier Carrasco, Andrew Hodgson, and Angelos Michaelides, "A molecular perspective of water at metal interfaces," Nature materials **11**, 667–674 (2012).
[6] Sabine Maier and Miquel Salmeron, "How does water wet a surface?" Accounts of chemical research **48**, 2783–2790 (2015).
[7] Olle Björneholm, Martin H Hansen, Andrew Hodgson, Li-Min Liu, David T Limmer, Angelos Michaelides, Philipp Pedevilla, Jan Rossmeisl, Huaze Shen, Gabriele Tocci, *et al.*, "Water at interfaces," Chemical reviews **116**, 7698–7726 (2016).
[8] Tomoko K Shimizu, Sabine Maier, Albert Verdaguer, Juan-Jesus Velasco-Velez, and Miquel Salmeron, "Water at surfaces and interfaces: From molecules to ice and bulk liquid," Progress in Surface Science **93**, 87–107 (2018).
[9] Guobing Zhou and Liangliang Huang, "A review of recent advances in computational and experimental analysis of first adsorbed water layer on solid substrate," Molecular Simulation **47**, 925–941 (2021).
[10] Ye Tian, Jiani Hong, Duanyun Cao, Sifan You, Yizhi Song, Bowei Cheng, Zhichang Wang, Dong Guan, Xinmeng Liu, Zhengpu Zhao, *et al.*, "Visualizing Eigen/Zundel cations and their interconversion in monolayer water on metal surfaces," Science **377**, 315–319 (2022).
[11] Shiwu Gao and Sheng Meng, "Water adsorption on solid surfaces: From single molecules to wetting structures," in *Encyclopedia of Solid-Liquid Interfaces (First Edition)*, edited by Klaus Wandelt and Gianlorenzo Bussetti (Elsevier, Oxford, 2024) first edition ed., pp. 136–149.
[12] P. A. Thiel, F. M. Hoffmann, and W. H. Weinberg, "Coadsorption of oxygen and water on Ru(001): Vibrational and structural properties," Phys. Rev. Lett. **49**, 501–504 (1982).
[13] Dale L Doering and Theodore E Madey, "The adsorption of water on clean and oxygen-dosed Ru(011)," Surface Science **123**, 305–337 (1982).
[14] P. A. Thiel, R. A. DePaola, and F. M. Hoffmann, "The vibrational spectra of chemisorbed molecular clusters: H_2O on Ru(001)," The Journal of Chemical Physics **80**, 5326–5331 (1984).
[15] G Pirug, C Ritke, and H.P Bonzel, "Adsorption of H_2O on Ru(001): I. bilayer and clusters," Surface Science **241**, 289–301 (1991).
[16] G. Held and D. Menzel, "The structure of the p($\sqrt{3}\times\sqrt{3}$)R30° bilayer of D_2O on Ru(001)," Surface Science **316**, 92–102 (1994).
[17] S. R. Puisto, T. J. Lerotholi, G. Held, and D. Menzel, "A refined

leed analysis of water on Ru(0001): An experimental test of the partial dissociation model," Surface Review and Letters **10**, 487–492 (2003).
[18] Peter J Feibelman, "Partial dissociation of water on Ru(0001)," Science **295**, 99–102 (2002).
[19] D.N. Denzler, Ch. Hess, R. Dudek, S. Wagner, Ch. Frischkorn, M. Wolf, and G. Ertl, "Interfacial structure of water on Ru(001) investigated by vibrational spectroscopy," Chemical Physics Letters **376**, 618–624 (2003).
[20] C Clay, S Haq, and A Hodgson, "Intact and dissociative adsorption of water on Ru(0001)," Chemical Physics Letters **388**, 89–93 (2004).
[21] S. Haq, C. Clay, G. R. Darling, G. Zimbitas, and A. Hodgson, "Growth of intact water ice on Ru(0001) between 140 and 160K: Experiment and density-functional theory calculations," Phys. Rev. B **73**, 115414 (2006).
[22] D.N Denzler, S Wagner, M Wolf, and G Ertl, "Isotope effects in the thermal desorption of water from Ru(001)," Surface Science **532-535**, 113–119 (2003), proceedings of the 7th International Conference on Nanometer-Scale Science and Technology and the 21st European Conference on Surface Science.
[23] K. Andersson, A. Nikitin, L. G. M. Pettersson, A. Nilsson, and H. Ogasawara, "Water dissociation on Ru(001): An activated process," Phys. Rev. Lett. **93**, 196101 (2004).
[24] N.S. Faradzhev, K.L. Kostov, P. Feulner, T.E. Madey, and D. Menzel, "Stability of water monolayers on Ru(0001): Thermal and electronically induced dissociation," Chemical Physics Letters **415**, 165–171 (2005).
[25] M. Tatarkhanov, E. Fomin, M. Salmeron, K. Andersson, H. Ogasawara, L. G. M. Pettersson, A. Nilsson, and J. I. Cerdá, "The structure of mixed H_2O-OH monolayer films on Ru(0001)," The Journal of Chemical Physics **129**, 154109 (2008).
[26] Jonas Weissenrieder, Anders Mikkelsen, Jesper N. Andersen, Peter J. Feibelman, and Georg Held, "Experimental evidence for a partially dissociated water bilayer on Ru(0001)," Phys. Rev. Lett. **93**, 196102 (2004).
[27] Mous Tatarkhanov, D. Frank Ogletree, Franck Rose, Toshiyuki Mitsui, Evgeny Fomin, Sabine Maier, Mark Rose, Jorge I. Cerdá, and Miquel Salmeron, "Metal- and hydrogen-bonding competition during water adsorption on Pd(111) and Ru(0001)," Journal of the American Chemical Society **131**, 18425–18434 (2009).
[28] Sabine Maier, Ingeborg Stass, Toshiyuki Mitsui, Peter J. Feibelman, Konrad Thürmer, and Miquel Salmeron, "Adsorbed water-molecule hexagons with unexpected rotations in islands on Ru(0001) and Pd(111)," Phys. Rev. B **85**, 155434 (2012).
[29] Sabine Maier, Ingeborg Stass, Jorge I. Cerdá, and Miquel Salmeron, "Unveiling the mechanism of water partial dissociation on Ru(0001)," Phys. Rev. Lett. **112**, 126101 (2014).
[30] Martin Schilling and R. Jürgen Behm, "Partial dissociation of water on Ru(0001) at low temperatures–adsorption, structure formation and hydrogen passivation effects," Surface Science **674**, 32–39 (2018).
[31] See Supplemental Material at http://link.aps.org/supplemental for the details of first-principles calculations, MTP construction and validation, energy barrier calculations, and path-integral and classical MD simulations, as well as the considered 43 water overlayer models used for calculating the adsorption energies in Fig. 1, which addtionally includes Refs. [78–86].
[32] A Michaelides, A Alavi, and DA King, "Different surface chemistries of water on Ru(0001): from monomer adsorption to partially dissociated bilayers," Journal of the American Chemical Society **125**, 2746–2755 (2003).
[33] Angelos Michaelides, Ali Alavi, and David A. King, "Insight into H_2O-ice adsorption and dissociation on metal surfaces from first-principles simulations," Phys. Rev. B **69**, 113404 (2004).
[34] Sheng Meng, E. G. Wang, and Shiwu Gao, "Water adsorption on metal surfaces: A general picture from density functional theory studies," Phys. Rev. B **69**, 195404 (2004).
[35] Sheng Meng, EG Wang, Ch Frischkorn, Martin Wolf, and Shiwu Gao, "Consistent picture for the wetting structure of water/Ru(0001)," Chemical physics letters **402**, 384–388 (2005).
[36] A. Michaelides, V. A. Ranea, P. L. de Andres, and D. A. King, "General model for water monomer adsorption on close-packed transition and noble metal surfaces," Phys. Rev. Lett. **90**, 216102 (2003).
[37] Peter J. Feibelman, "A wetting layer breaks the ice rules," Chemical Physics Letters **410**, 120–124 (2005).
[38] Mark Gallagher, Ahmed Omer, George R Darling, and Andrew Hodgson, "Order and disorder in the wetting layer on Ru(0001)," Faraday Discussions **141**, 231–249 (2009).
[39] Javier Carrasco, Biswajit Santra, Jiří Klimeš, and Angelos Michaelides, "To wet or not to wet? dispersion forces tip the balance for water ice on metals," Phys. Rev. Lett. **106**, 026101 (2011).
[40] Jeffrey A Herron, Scott Tonelli, and Manos Mavrikakis, "Atomic and molecular adsorption on Ru(0001)," Surface science **614**, 64–74 (2013).
[41] Alexander V. Shapeev, "Moment tensor potentials: a class of systematically improvable interatomic potentials," Multiscale Modeling & Simulation **14**, 1153–1173 (2016).
[42] Peitao Liu, Jiantao Wang, Noah Avargues, Carla Verdi, Andreas Singraber, Ferenc Karsai, Xing-Qiu Chen, and Georg Kresse, "Combining machine learning and many-body calculations: coverage-dependent adsorption of CO on Rh(111)," Physical Review Letters **130**, 078001 (2023).
[43] Mingfeng Liu, Jiantao Wang, Junwei Hu, Peitao Liu, Haiyang Niu, Xuexi Yan, Jiangxu Li, Haile Yan, Bo Yang, Yan Sun, Chunlin Chen, Georg Kresse, Liang Zuo, and Xing-Qiu Chen, "Layer-by-layer phase transformation in Ti_3O_5 revealed by machine-learning molecular dynamics simulations," Nature Communications **15**, 3079 (2024).
[44] Ryosuke Jinnouchi, Jonathan Lahnsteiner, Ferenc Karsai, Georg Kresse, and Menno Bokdam, "Phase transitions of hybrid perovskites simulated by machine-learning force fields trained on the fly with bayesian inference," Physical Review Letters **122**, 225701 (2019).
[45] Ryosuke Jinnouchi, Ferenc Karsai, and Georg Kresse, "On-the-fly machine learning force field generation: application to melting points," Physical Review B **100**, 014105 (2019).
[46] G. Kresse and J. Hafner, "Ab initio molecular dynamics for liquid metals," Phys. Rev. B **47**, 558–561 (1993).
[47] G. Kresse and J. Furthmüller, "Efficient iterative schemes for ab initio total-energy calculations using a plane-wave basis set," Phys. Rev. B **54**, 11169–11186 (1996).
[48] Ivan S Novikov, Konstantin Gubaev, Evgeny V Podryabinkin, and Alexander V Shapeev, "The MLIP package: moment tensor potentials with MPI and active learning," Machine Learning: Science and Technology **2**, 025002 (2021).
[49] B. Hammer, L. B. Hansen, and J. K. Nørskov, "Improved adsorption energetics within density-functional theory using revised perdew-burke-ernzerhof functionals," Phys. Rev. B **59**, 7413–7421 (1999).
[50] Stefan Grimme, Jens Antony, Stephan Ehrlich, and Helge Krieg, "A consistent and accurate ab initio parametrization of density functional dispersion correction (DFT-D) for the 94 ele-

ments H-Pu," The Journal of Chemical Physics **132**, 154104 (2010).
[51] Jianwei Sun, Adrienn Ruzsinszky, and John P. Perdew, "Strongly constrained and appropriately normed semilocal density functional," Phys. Rev. Lett. **115**, 036402 (2015).
[52] John P. Perdew, Kieron Burke, and Matthias Ernzerhof, "Generalized gradient approximation made simple," Phys. Rev. Lett. **77**, 3865–3868 (1996).
[53] Jiří Klimeš, David R Bowler, and Angelos Michaelides, "Chemical accuracy for the van der waals density functional," Journal of Physics: Condensed Matter **22**, 022201 (2009).
[54] Jiantao Wang, Peitao Liu, Heyu Zhu, Mingfeng Liu, Hui Ma, Yun Chen, Yan Sun, and Xing-Qiu Chen, "Efficient moment tensor machine-learning interatomic potential for accurate description of defects in ni-al alloys," arXiv:2411.01282 (2024).
[55] G. Held, W. Braun, H.-P. Steinrück, S. Yamagishi, S. J. Jenkins, and D. A. King, "Light-atom location in adsorbed benzene by experiment and theory," Phys. Rev. Lett. **87**, 216102 (2001).
[56] Aidan P. Thompson, H. Metin Aktulga, Richard Berger, Dan S. Bolintineanu, W. Michael Brown, Paul S. Crozier, Pieter J. in 't Veld, Axel Kohlmeyer, Stan G. Moore, TRung Dac Nguyen, Ray Shan, Mark J. Stevens, Julien Tranchida, Christian Trott, and Steven J. Plimpton, "Lammps-a flexible simulation tool for particle-based materials modeling at the atomic, meso, and continuum scales," Computer Physics Communications **271**, 108171 (2022).
[57] Donald G. Truhlar, Bruce C. Garrett, and Stephen J. Klippenstein, "Current status of transition-state theory," The Journal of Physical Chemistry **100**, 12771–12800 (1996).
[58] Dominik Marx and Michele Parrinello, "Ab initio path integral molecular dynamics: Basic ideas," The Journal of Chemical Physics **104**, 4077–4082 (1996).
[59] Magali Benoit, Dominik Marx, and Michele Parrinello, "Tunnelling and zero-point motion in high-pressure ice," Nature **392**, 258–261 (1998).
[60] Dominik Marx, Mark E. Tuckerman, Jürg Hutter, and Michele Parrinello, "The nature of the hydrated excess proton in water," Nature **397**, 601–604 (1999).
[61] T. Kumagai, M. Kaizu, S. Hatta, H. Okuyama, T. Aruga, I. Hamada, and Y. Morikawa, "Direct observation of hydrogen-bond exchange within a single water dimer," Phys. Rev. Lett. **100**, 166101 (2008).
[62] Joseph A. Morrone, Lin Lin, and Roberto Car, "Tunneling and delocalization effects in hydrogen bonded systems: A study in position and momentum space," The Journal of Chemical Physics **130**, 204511 (2009).
[63] Xin-Zheng Li, Matthew I. J. Probert, Ali Alavi, and Angelos Michaelides, "Quantum nature of the proton in water-hydroxyl overlayers on metal surfaces," Phys. Rev. Lett. **104**, 066102 (2010).
[64] Xin-Zheng Li, Brent Walker, and Angelos Michaelides, "Quantum nature of the hydrogen bond," Proceedings of the National Academy of Sciences **108**, 6369–6373 (2011).
[65] Ji Chen, Xin-Zheng Li, Qianfan Zhang, Matthew I. J. Probert, Chris J. Pickard, Richard J. Needs, Angelos Michaelides, and Enge Wang, "Quantum simulation of low-temperature metallic liquid hydrogen," Nature Communications **4**, 2064 (2013).
[66] Yexin Feng, Ji Chen, Xin-Zheng Li, and Enge Wang, "Ab initio path-integral molecular dynamics and the quantum nature of hydrogen bonds*," Chinese Physics B **25**, 013104 (2015).
[67] Jing Guo, Jing-Tao Lü, Yexin Feng, Ji Chen, Jinbo Peng, Zeren Lin, Xiangzhi Meng, Zhichang Wang, Xin-Zheng Li, En-Ge Wang, and Ying Jiang, "Nuclear quantum effects of hydrogen bonds probed by tip-enhanced inelastic electron tunneling," Science **352**, 321–325 (2016).
[68] Michele Ceriotti, Wei Fang, Peter G. Kusalik, Ross H. McKenzie, Angelos Michaelides, Miguel A. Morales, and Thomas E. Markland, "Nuclear quantum effects in water and aqueous systems: Experiment, theory, and current challenges," Chemical Reviews **116**, 7529–7550 (2016).
[69] Jing Guo, Xin-Zheng Li, Jinbo Peng, En-Ge Wang, and Ying Jiang, "Atomic-scale investigation of nuclear quantum effects of surface water: Experiments and theory," Progress in Surface Science **92**, 203–239 (2017).
[70] Mohan Chen, Lixin Zheng, Biswajit Santra, Hsin-Yu Ko, Robert A. DiStasio Jr, Michael L. Klein, Roberto Car, and Xifan Wu, "Hydroxide diffuses slower than hydronium in water because its solvated structure inhibits correlated proton transfer," Nature Chemistry **10**, 413–419 (2018).
[71] Thomas E. Markland and Michele Ceriotti, "Nuclear quantum effects enter the mainstream," Nature Reviews Chemistry **2**, 0109 (2018).
[72] Wei Fang, Ji Chen, Yexin Feng, Xin-Zheng Li, and Angelos Michaelides, "The quantum nature of hydrogen," International Reviews in Physical Chemistry **38**, 35–61 (2019).
[73] Bingqing Cheng, Edgar A. Engel, Jörg Behler, Christoph Dellago, and Michele Ceriotti, "Ab initio thermodynamics of liquid and solid water," Proceedings of the National Academy of Sciences **116**, 1110–1115 (2019).
[74] Jinggang Lan, Vladimir V. Rybkin, and Marcella Iannuzzi, "Ionization of water as an effect of quantum delocalization at aqueous electrode interfaces," The Journal of Physical Chemistry Letters **11**, 3724–3730 (2020).
[75] Sigbjørn Løland Bore and Francesco Paesani, "Realistic phase diagram of water from "first principles" data-driven quantum simulations," Nature Communications **14**, 3349 (2023).
[76] Mischa Flór, David M. Wilkins, Miguel de la Puente, Damien Laage, Giuseppe Cassone, Ali Hassanali, and Sylvie Roke, "Dissecting the hydrogen bond network of water: Charge transfer and nuclear quantum effects," Science **0**, eads4369 (2024).
[77] https://github.com/wftao1995/Water-Dissociation-on-Ru-0001-Dataset.
[78] P. E. Blöchl, "Projector augmented-wave method," Phys. Rev. B **50**, 17953–17979 (1994).
[79] G. Kresse and D. Joubert, "From ultrasoft pseudopotentials to the projector augmented-wave method," Phys. Rev. B **59**, 1758–1775 (1999).
[80] Katrin Forster-Tonigold and Axel Groß, "Dispersion corrected RPBE studies of liquid water," The Journal of Chemical Physics **141**, 064501 (2014).
[81] Tobias Morawietz, Andreas Singraber, Christoph Dellago, and Jörg Behler, "How van der waals interactions determine the unique properties of water," Proceedings of the National Academy of Sciences **113**, 8368–8373 (2016).
[82] John W. Arblaster, "Crystallographic properties of ruthenium," Platinum Metals Review **57**, 127–136 (2013).
[83] Peter J. Feibelman, "Lattice match in density functional calculations: ice Ih vs. β-AgI," Phys. Chem. Chem. Phys. **10**, 4688–4691 (2008).
[84] Di Zhao, Feng Liu, Xiangmei Duan, and Deyan Sun, "Intrinsic disorder of dangling OH-bonds in the first water layer on noble metal surfaces," Computational Materials Science **201**, 110863 (2022).
[85] Graeme A Henkelman, Blas Pedro Uberuaga, and Hannes Jónsson, "A climbing image nudged elastic band method for finding saddle points and minimum energy paths," Journal of Chemical Physics **113**, 9901–9904 (2000).
[86] Nosé Shuichi, "Constant temperature molecular dynamics

methods," Progress of Theoretical Physics Supplement **103**, 1– 46 (1991).

Supplemental Material to "Quantum Delocalization Enables Water Dissociation on Ru(0001)"

Yu Cao,[1,2,*] Jiantao Wang,[1,2,*] Mingfeng Liu,[1] Yan Liu,[1,2] Hui Ma,[1]
Cesare Franchini,[3,4] Yan Sun,[1] Georg Kresse,[3] Xing-Qiu Chen,[1,†] and Peitao Liu[1,‡]

[1]*Shenyang National Laboratory for Materials Science, Institute of Metal Research, Chinese Academy of Sciences, 110016 Shenyang, China*
[2]*School of Materials Science and Engineering, University of Science and Technology of China, 110016 Shenyang, China*
[3]*University of Vienna, Faculty of Physics and Center for Computational Materials Science, Kolingasse 14-16, A-1090 Vienna, Austria*
[4]*Dipartimento di Fisica e Astronomia, Università di Bologna, 40127 Bologna, Italy*

* These authors contribute equally to this work.
† xingqiu.chen@imr.ac.cn
‡ ptliu@imr.ac.cn

I. FIRST-PRINCIPLES CALCULATIONS

The first-principles calculations were performed using the Vienna *ab initio* simulation package (VASP) [1, 2]. The generalized gradient approximation of revised Perdew-Burke-Ernzerhof functional (RPBE) [3] was used for the exchange-correlation functional [3]. The projector augmented wave (PAW) pseudopotentials [4, 5] (`Ru_sv`, `H` and `O`) were adopted. A plane wave cutoff of 450 eV and a Γ-centered k-point grid with a spacing of 0.201 $Å^{-1}$ between k points were employed. The Gaussian smearing method with a smearing width of 0.05 eV was used. The electronic optimization was performed until the total energy difference between two consecutive iterations was less than 10^{-6} eV. The structures were optimized until the forces were smaller than 0.02 eV/Å. The van der Waals (VdWs) interaction was accounted for via the D3 method of Grimme *et al.* [6] with standard zero damping.

The water adsorption energy on Ru(0001) (E_{ads}, in eV/H_2O) was calculated as

$$E_{ads} = (E_{\text{total}} - E_{\text{surf}} - \text{n}E_{\text{H}_2\text{O}})/n, \tag{1}$$

where E_{total} is the total energy of the water overlayer on Ru(0001), E_{surf} is the total energy of the clean surface, n is the number of adsorbed H_2O molecules, and $E_{\text{H}_2\text{O}}$ is the total energy of the H_2O molecule. The slab was modeled using 5 layers with the bottom three layers fixed and a vacuum width of 15 Å.

The sublimation energy of bulk ice-Ih (E_{sub}, in eV/H_2O) was calculated as

$$E_{sub} = (E_{\text{ice-Ih}} - \text{n}E_{\text{H}_2\text{O}})/n, \tag{2}$$

where $E_{\text{ice-Ih}}$ is the total energy of bulk ice-Ih, n is the number of H_2O formula units in the bulk ice-Ih, and $E_{\text{H}_2\text{O}}$ is the total energy of the H_2O molecule.

The surface energy of Ru(0001) (E_{sf}) was calculated as

$$E_{sf} = \frac{1}{2A}(E_{\text{slab}} - NE_{\text{bulk}}), \tag{3}$$

where E_{slab} is the total energy of the slab, E_{bulk} is the total energy per atom of bulk Ru, N is the number of Ru atoms in the slab, and A is the surface area.

II. ASSESSMENT OF EXCHANGE-CORRELATION FUNCTIONALS

To assess the performance of the RPBE+D3 method [3, 6], we computed the lattice parameters of bulk Ru, surface energy of Ru(0001), the sublimation energy of ice-Ih, and the adsorption energy as well as the vertical distances between Ru-O and O-O of seven selected water overlayer configurations including the H-up bilayer (cfg18), H-down bilayer (cfg15), half-dissociated (cfg42) [7], extended chains (cfg32) [8], modified half-dissociated (cfg41) [7], two-linear-chains (cfg25) [8], and four-arc-chains (cfg28) [8]. The configurations were denoted according to Figure 1 in the main text. Their crystal structures were illustrated in Fig. S2. The RPBE+D3 computed results were compared with those predicted by PBE+D3 [9], optB88-vdW [10], and SCAN [11], and summarized in Table S1. Furthermore, Figure S1 depicted the vertical distances between Ru-O and O-O and water adsorption energies predicted by four functionals. It is evident that the four functionals investigated yielded largely similar outcomes. Because of the improved description for the adsorption energetics by RPBE [3] and the excellent description of the water behavior by RPBE+D3 [12, 13], we ultimately opted for the RPBE+D3 functional in this work.

Table S1. The adsorption energies (E_{ads}, in eV/H_2O) and the vertical distances between Ru-O (in Å) and O-O (in Å) of seven selected water overlayer configurations, the sublimation energy of ice-Ih (E_{sub}, in eV/H_2O), the lattice parameters of bulk Ru (in Å), and the surface energy of Ru(0001) (E_{sf}, in eV/Å^2) predicted by PBE+D3, optB88-vdW, SCAN, and RPBE+D3 methods. Note that the experimental lattice constants of bulk Ru at 0 K are a=b=2.703 Å and c=4.274 Å [14], and the experimentally measured sublimation energy of ice-Ih is −0.61 eV/H_2O [15].

		$\sqrt{3}\times\sqrt{3}$			$\sqrt{3}\times 2\sqrt{3}$	$2\sqrt{3}\times 2\sqrt{3}$			ice-Ih E_{sub}	Lattice	E_{sf}
		cfg18 [16]	cfg15 [16]	cfg42 [7]	cfg32[17]	cfg41 [7]	cfg25 [8]	cfg28 [8]	(eV/H_2O)	parameters	(eV/Å^2)
PBE+D3	E_{ads}	-0.72	-0.72	-1.02	-0.84	-0.99	-0.80	-0.81	-0.74	a=2.69	0.22
	Ru-O	2.39	2.45	2.07	2.32	2.08	2.32	2.29		b=2.69	
	O-O	0.75	0.54	0.05	0.92	0.084	0.80	0.92		c=4.28	
optB88-vdW	E_{ads}	-0.70	-0.67	-0.98	-0.79	-0.96	-0.74	-0.76	-0.71	a=2.72	0.18
	Ru-O	2.45	2.51	2.08	2.34	2.10	2.35	2.31		b=2.72	
	O-O	0.79	0.54	0.05	0.92	0.087	0.81	0.94		c=4.31	
SCAN	E_{ads}	-0.68	-0.65	-1.01	-0.79	-0.99	-0.73	-0.75	-0.72	a=2.69	0.19
	Ru-O	2.47	2.55	2.06	2.33	2.07	2.33	2.27		b=2.69	
	O-O	0.83	0.47	0.05	1.00	0.12	0.86	1.00		c=4.26	
RPBE+D3	E_{ads}	-0.60	-0.58	-0.83	-0.69	-0.82	-0.66	-0.67	-0.62	a=2.69	0.22
	Ru-O	2.49	2.60	2.08	2.37	2.11	2.39	2.33		b=2.69	
	O-O	0.81	0.47	0.06	0.90	0.09	0.83	0.97		c=4.27	

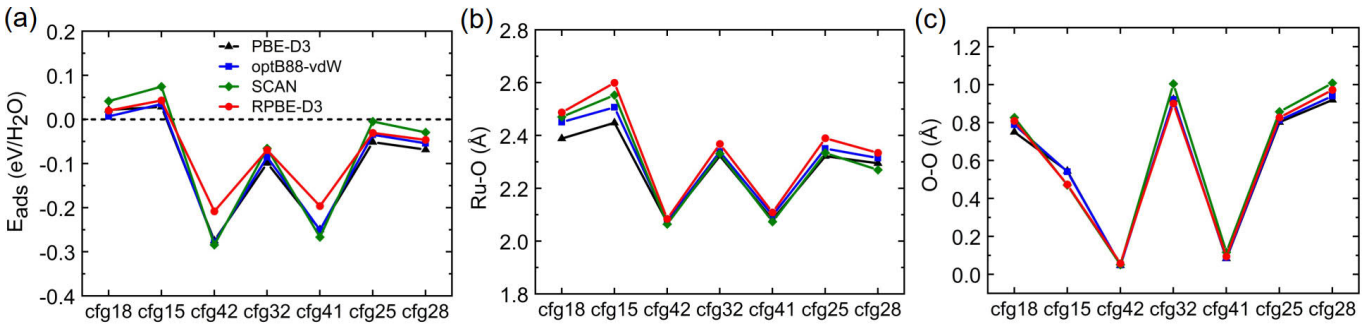

Figure S1. (a) The relative energies of water adsorption with respect to the sublimation energy of ice-Ih predicted by four functionals. (b) and (c) depict the vertical distances between Ru-O and O-O, respectively.

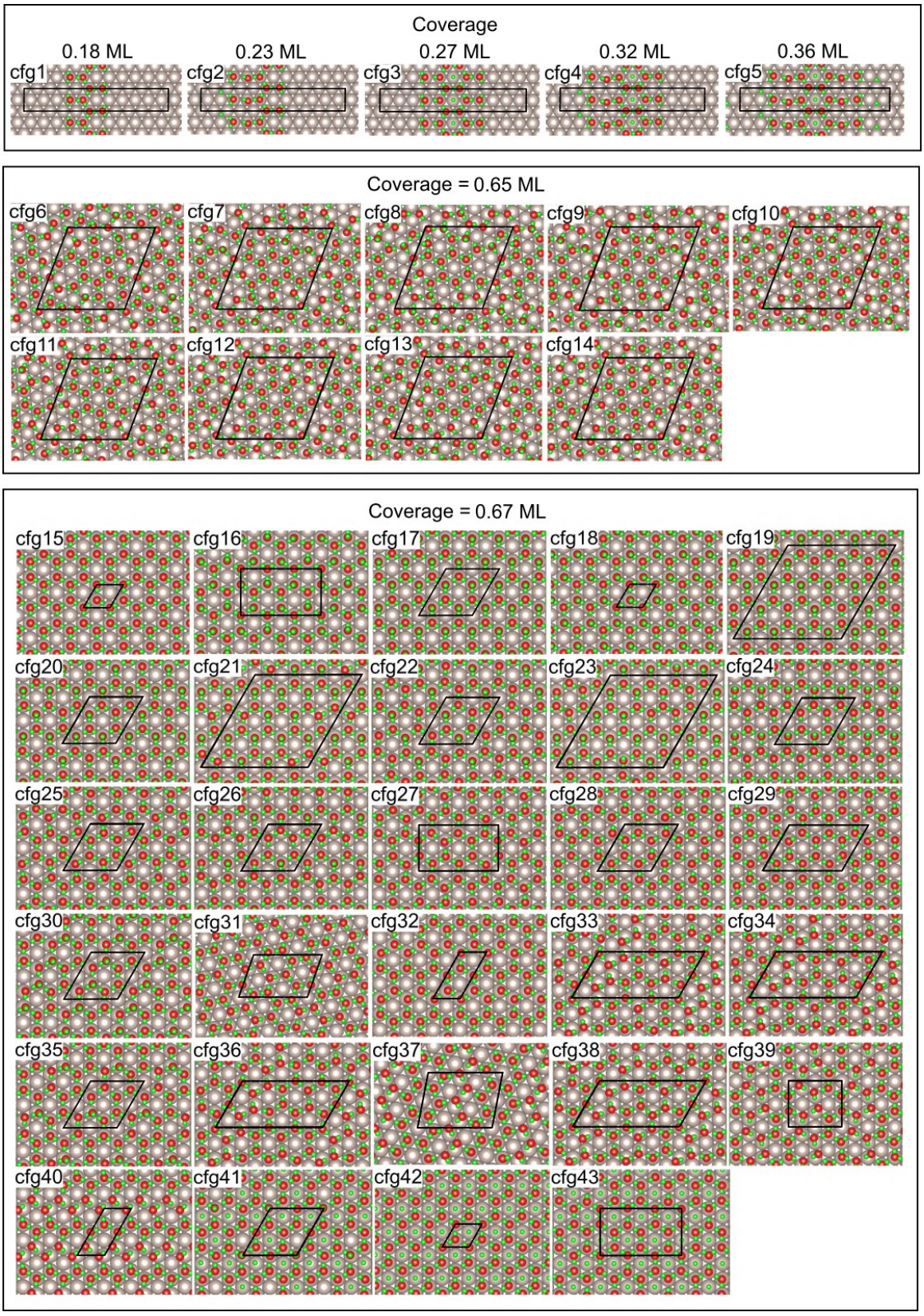

Figure S2. The considered 43 water overlayer configurations on Ru(0001) with various coverages, for which the adsorption energies were calculated and displayed in Figure 1 of the main text. The configurations from cfg1 to cfg4 were take from Ref. [18]. The configuration cfg5 was extracted from Ref. [18, 19]. The configurations of cfg6-cfg14, cfg17, cfg19-cfg24, cfg26, cfg30, and cfg35 were taken from Ref. [20]. The configurations of cfg15, cfg16, cfg18, and cfg43 were extracted from Ref. [16]. The configuration of cfg32 was obtained from Ref. [17]. The configurations of cfg25, cfg27-cfg29, cfg31, cfg33-cfg34, and cfg36-cfg39 were derived from Ref. [8]. The configurations of cfg41 and cfg42 were obtained from Ref. [7]. The Ru, O, and H atoms are represented by brown, red, and green spheres, respectively. The black lines indicate the unit cell.

III. TRAINING AND VALIDATION OF MOMENT TENSOR POTENTIAL

The training dataset construction followed the scheme outlined in our previous works [21, 22]. Specifically, the training structures were initially sampled using an on-the-fly active learning scheme based on the Bayesian linear regression [23, 24]. This enabled us to efficiently sample the phase space and automatically collect the representative training structures during the molecular dynamics (MD) simulations. The cutoff radius for the three-body descriptors and the width of the Gaussian functions used for broadening the atomic distributions of the three-body descriptors were set to 6 Å and 0.5 Å, respectively. The number of radial basis functions used to expand the radial descriptor was set to 10. Then, the training dataset was expanded iteratively using the active learning method implemented in the MLIP package [25]. For the training of the moment tensor potential (MTP), a cutoff radius of 6.0 Å was used, and the number of radial basis was set to be 8. The MD samplings were conducted by heating the water overlayers at various coverages from 10 K to 400 K using the NVT canonical ensemble. Additionally, configurations derived from path-integral molecular dynamics simulations were incorporated into the training dataset, guided by the active learning framework [25].

The eventual training dataset contained 6,813 structures including water molecule, bulk ice-Ih, bulk Ru, and clean Ru(0001) surface, as well as intact and dissociated water overlayers at various coverages up to 2/3 monolayer (ML) (see Table S2). To enhance efficiency, the ultimate MTP was fitted with the optimized basis sets by refining the contraction process of moment tensors using our in-house code (IMR-MLP) [26]. The MTP was validated on a test dataset containing 600 structures including bulk Ru, clean Ru(0001) surface, intact and half-dissociated water overlayers at 2/3 ML (see Table S3). These test structures were randomly sampled from additional MD simulations. The kernel principal component analysis on both the training and validation datasets were presented in Fig. S3(a). The root-mean-square errors in energies and forces for the training and validation datasets were displayed in Table S4, while the parity plots for MTP-predicted energies and forces against DFT results were depicted in Fig. S3(b) and Fig. S3(c), showcasing the high accuracy of the generated MTP.

Table S2. Summary of the structures included in the training dataset.

H_2O coverages (ML)	Structure type	Number of structures
—	Bulk ice-Ih of 36-atom cell	306
—	Bulk Ru of 54-atom cell	111
0/3	Clean $\sqrt{3}\times\sqrt{3}$ Ru(0001)	183
0/6	Clean $\sqrt{3}\times2\sqrt{3}$ Ru(0001)	287
0/12	Clean $2\sqrt{3}\times2\sqrt{3}$ Ru(0001)	176
2/3	$2H_2O@\sqrt{3}\times\sqrt{3}$ Ru(0001)	1329
4/6	$4H_2O@\sqrt{3}\times2\sqrt{3}$ Ru(0001)	371
1/9	$1H_2O@3\times3$ Ru(0001)	28
2/9	$2H_2O@3\times3$ Ru(0001)	81
3/9	$3H_2O@3\times3$ Ru(0001)	89
4/9	$4H_2O@3\times3$ Ru(0001)	106
6/9	$6H_2O@3\times3$ Ru(0001)	679
7/9	$7H_2O@3\times3$ Ru(0001)	120
8/12	$8H_2O@2\sqrt{3}\times2\sqrt{3}$ Ru(0001)	684
8/12	$8H_2O@3\times2\sqrt{3}$ Ru(0001)	1439
10/15	$10H_2O@3\times\sqrt{21}$ Ru(0001)	27
12/18	$12H_2O@3\times3\sqrt{3}$ Ru(0001)	226
4/22	$4H_2O@11\times\sqrt{3}$ Ru(0001)	2
5/22	$5H_2O@11\times\sqrt{3}$ Ru(0001)	62
6/22	$6H_2O@11\times\sqrt{3}$ Ru(0001)	15
7/22	$7H_2O@11\times\sqrt{3}$ Ru(0001)	41
8/22	$8H_2O@11\times\sqrt{3}$ Ru(0001)	150
8/24	$8H_2O@3\times4\sqrt{3}$ Ru(0001)	121
10/24	$10H_2O@3\times4\sqrt{3}$ Ru(0001)	117
16/24	$16H_2O@3\times4\sqrt{3}$ Ru(0001)	28
12/32	$12H_2O@8\times2\sqrt{3}$ Ru(0001)	4
24/36	$24H_2O@6\times3\sqrt{3}$ Ru(0001)	21
26/40	$26H_2O@\sqrt{37}\times\sqrt{37}$ Ru(0001)	10
Total		6813

Table S3. Summary of the structures included in the validation dataset.

H_2O coverages (ML)	Structure type	Number of structures
—	Bulk Ru of 54-atom cell	100
0/12	Clean 2 $\sqrt{3}$×2 $\sqrt{3}$ Ru(0001)	100
8/12	8H_2O@2 $\sqrt{3}$×2 $\sqrt{3}$ Ru(0001)	400
Total		600

Table S4. The root-mean-square errors (RMSEs) in energies per atom (meV/atom) and forces (eV/Å) for the training and validation datasets.

	Training dataset (6,813 structures)	Validation dataset (600 structures)
Energy	0.764	1.019
Force	0.063	0.059

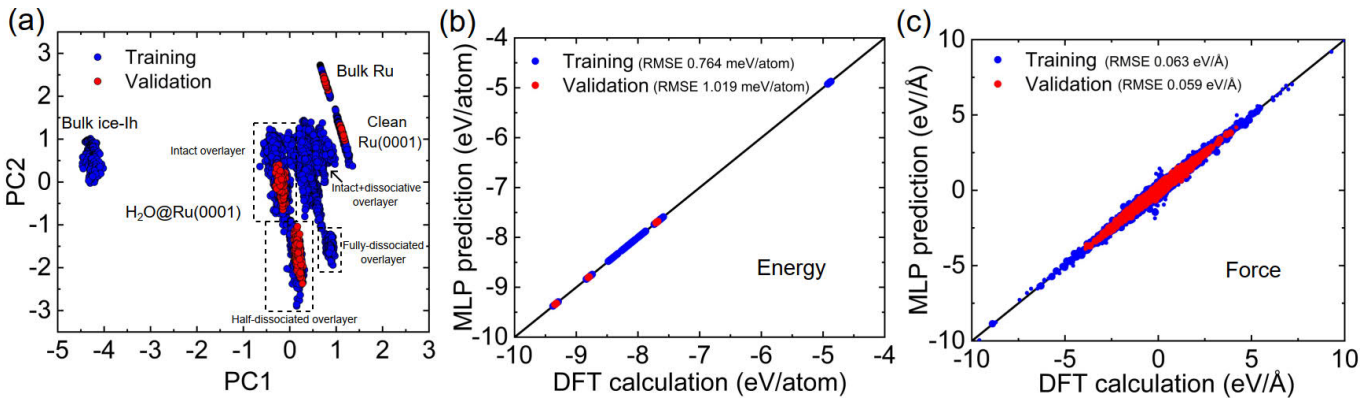

Figure S3. (a) Kernel principal component analysis map of training structures (blue circles) and validation structures (red circles). (b) Machine-learning potential (MLP) predicted energies versus DFT results. (c) MLP predicted forces versus DFT results.

IV. EXAMINING DISORDER EFFECTS

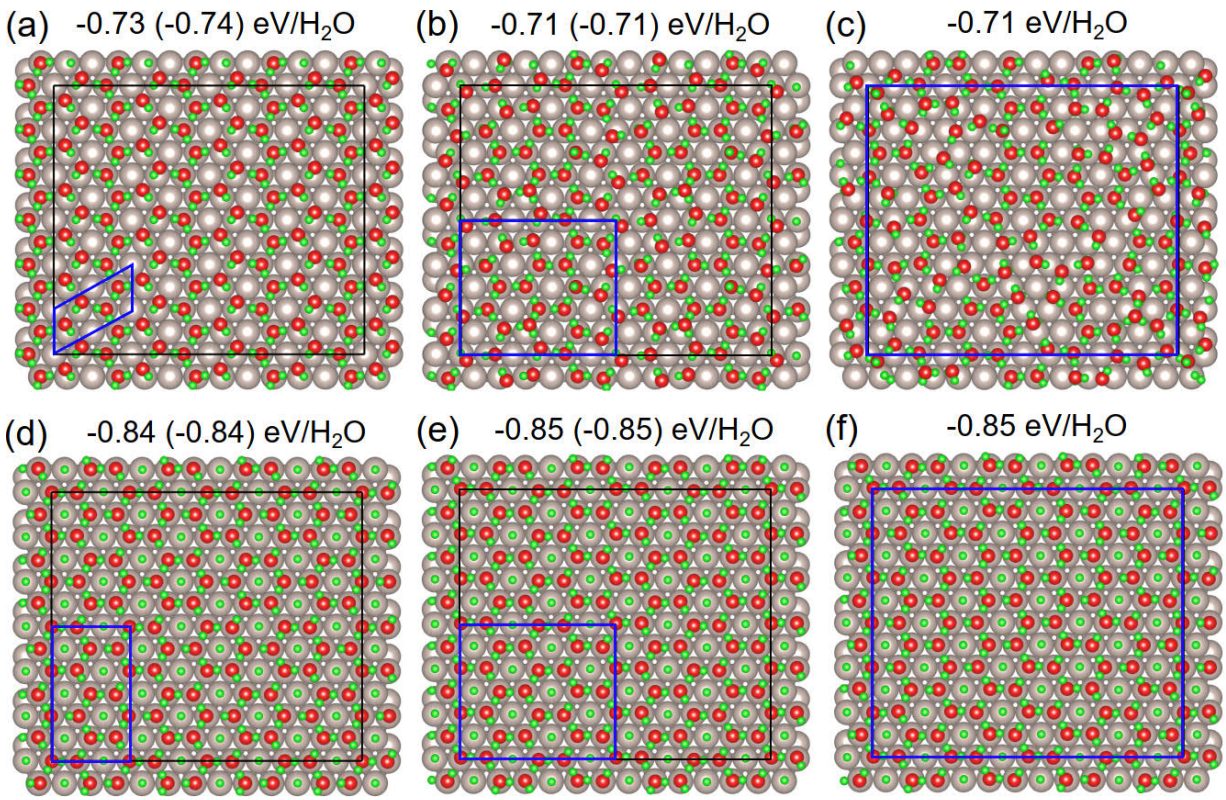

Figure S4. (a) The extended chains model with a unit cell of $\sqrt{3}\times 2\sqrt{3}$ (i.e., cfg 40 [17]). (b) The extended chains model with a unit cell of $6\times 3\sqrt{3}$. (c) The extended chains model with a unit cell of $12\times 6\sqrt{3}$. (d) The half-dissociated model with a unit cell of $3\sqrt{3}\times 3$ (i.e., cfg 43 [16]). (e) The half-dissociated model with a unit cell of $6\times 3\sqrt{3}$. (f) The half-dissociated model with a unit cell of $12\times 6\sqrt{3}$. The blue lines indicate the unit cell. Note that (b), (c), (e), and (f) depict the lowest-energy configurations, each of which was identified from 90 independent simulated annealing MD simulations followed by structural relaxations. All the configurations are expanded to the $12\times 6\sqrt{3}$ supercell for aiding the visibility. The MTP and DFT (in brackets) predicted adsorption energies (in eV/H_2O) are indicated above each configuration.

V. ENERGY BARRIER FOR WATER DISSOCIATION AT 0 K

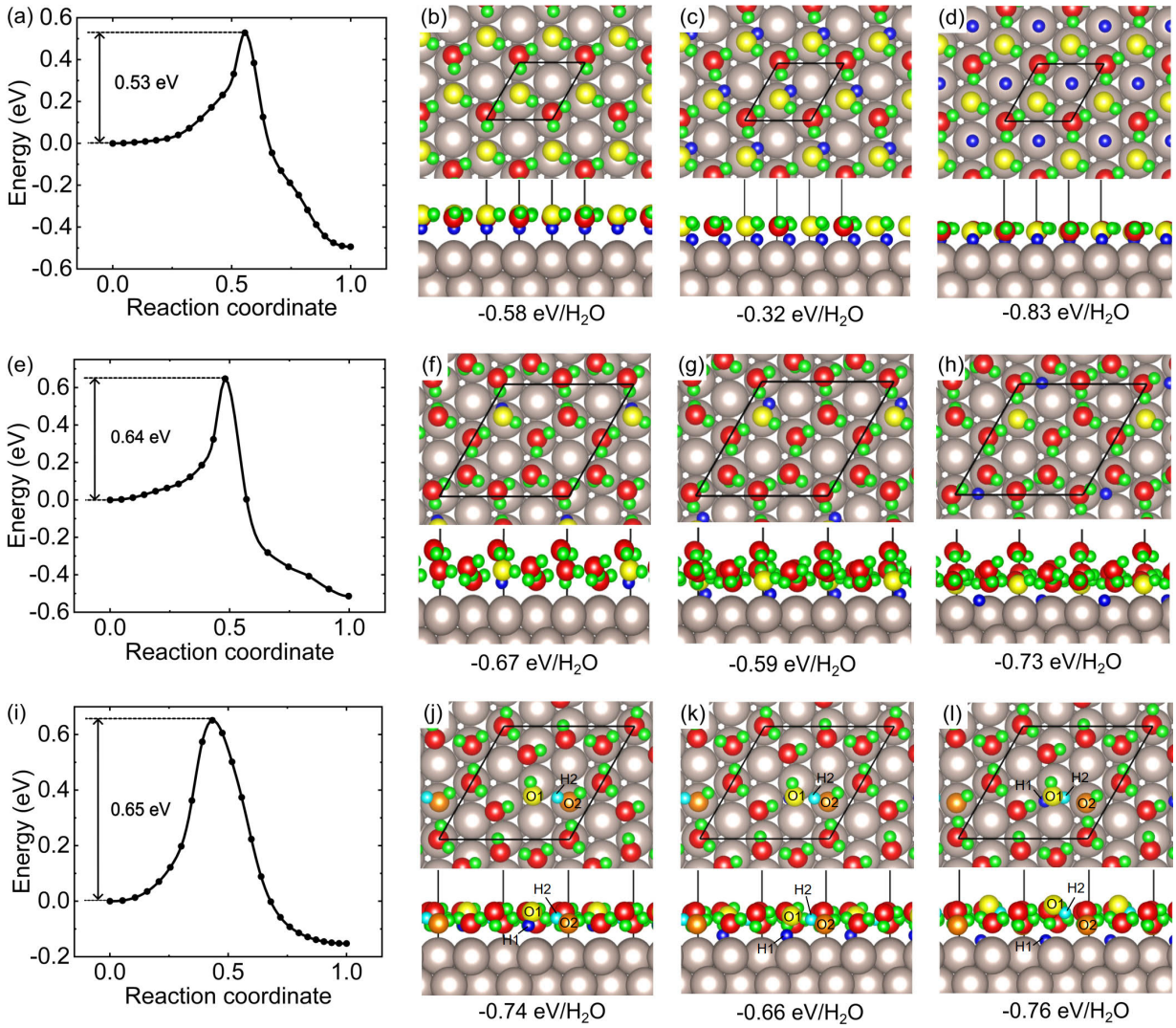

Figure S5. (a) The MTP-predicted energy profile for the dissociation of half the water in the H-down bilayer structure using the climbing image nudged elastic band method [27]. Panels (b), (c), and (d) depict the initial, transitional, and final configurations, respectively, corresponding to the dissociation process in panel (a). (e) The MTP-predicted energy profile for the dissociation of 1/8 of the water in the H-down bilayer structure. Panels (f), (g), and (h) depict the initial, transitional, and final configurations, respectively, corresponding to the dissociation process in panel (e). (i) The MTP-predicted energy profile for the dissociation of 1/8 of the water in the extended chain structure. Panels (j), (k), and (l) depict the initial, transitional, and final configurations, respectively, corresponding to the dissociation process in panel (i). Note that the brown spheres represent Ru atoms, while the red and yellow spheres stand for oxygen atoms of intact and dissociated water molecules, respectively. Moreover, the green and blue spheres denote the hydrogen atoms in intact water molecules and the dissociative hydrogen atom, respectively. In panels (j), (k), and (l), the cyan sphere indicates the hydrogen atom (referred to as "H2") participating in an indirect dissociation process. Specifically, two H_2O molecules (labeled O1 and O2) are involved in the dissociation process (i). The MTP predicted adsorption energies (in eV/H_2O) are indicated below each configuration.

VI. ENERGY BARRIER FOR WATER DESORPTION AT 0 K

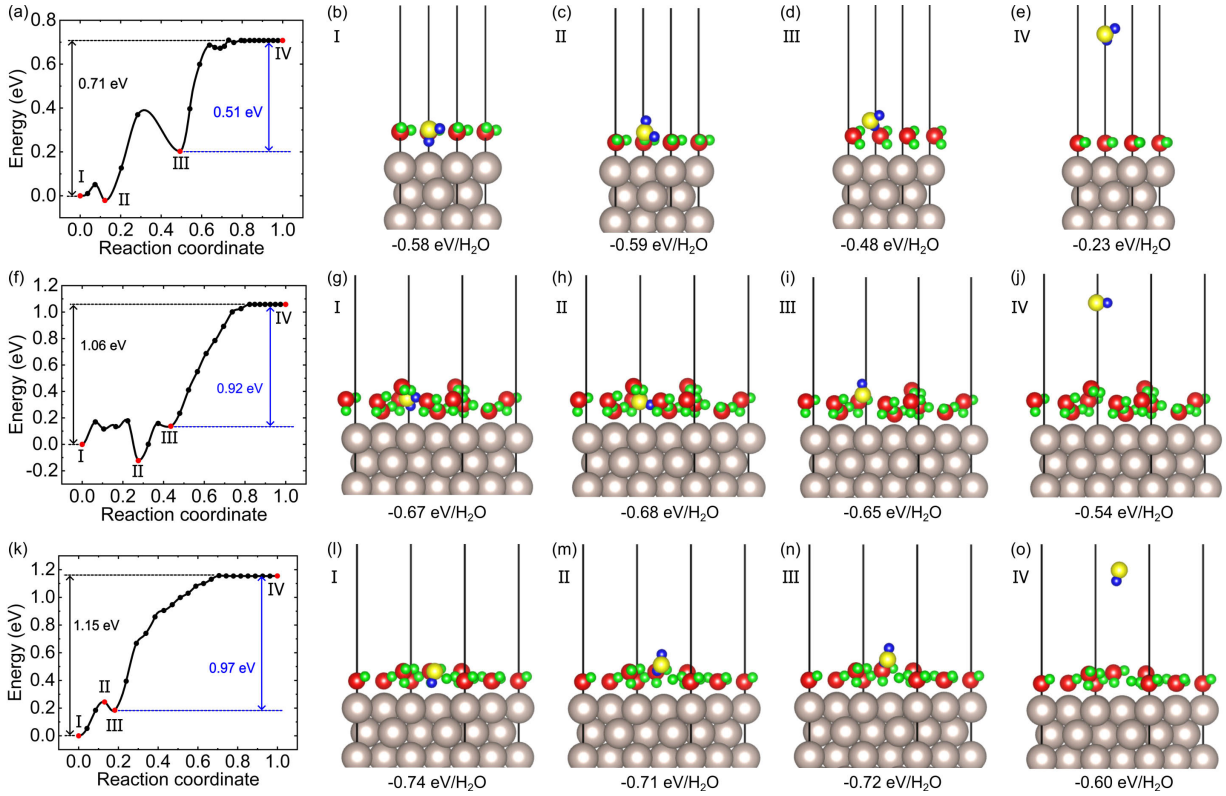

Figure S6. (a) The MTP-predicted energy profile for the desorption of half the water in the H-down bilayer structure using the climbing image nudged elastic band method [27]. Panels (b), (c), (d), and (e) depict the configurations marked in panel (a). (f) The MTP-predicted energy profile for the desorption of 1/8 of the water in the H-down bilayer structure. Panels (g), (h), (i), and (j) depict the configurations marked in panel (f). (k) The MTP-predicted energy profile for the desorption of 1/8 of the water in the extended chain structure. Panels (l), (m), (n), and (o) depict the configurations marked in panel (k). In panels (a), (f), and (k), the black values indicate desorption energies, while the blue values represent desorption energy barriers for the rate-determining step. Note that the H-down bilayer structure is a metastable configuration as compared to the extended chain structure. The atomic representations are as follows: brown spheres for Ru atoms, red and yellow spheres for oxygen atoms in intact and desorbed water molecules, respectively, and green and blue spheres for hydrogen atoms in intact and desorbed water molecules, respectively. Below each configuration, the MTP-predicted adsorption energies are provided.

VII. PATH-INTEGRAL AND CLASSICAL MOLECULAR DYNAMICS SIMULATIONS

The classical molecular dynamics (MD) and path-integral molecular dynamics (PIMD) simulations were conducted using the LAMMPS code [28] in the NVT canonical ensemble. Unless explicitly stated otherwise, all simulations were conducted at room temperature (300 K). We note that, the relatively high simulated temperature we employed was intended to accelerate the dynamics of the simulation. The temperature was controlled using a Nosé-Hoover thermostat [29]. The time step was set to 0.5 fs. In the PIMD simulations, each nucleus was represented by 16 beads and the statistical analyses were derived by averaging these 16 beads. Note that we also conducted the PIMD simulations employing 32 beads and the similar water dissociation was observed [see Fig. S7(e)]. A $6 \times 4\sqrt{3}$ supercell of the most stable intact overlayer configuration (i.e., extended chains model) was employed as the initial structure. Figs. S7(a)-(e) illustrate the time evolution of the number of OH, H_2O, and H_3O species in a series of independent MD and PIMD simulations. Fig. S7(f) shows the time evolution of the oxygen atom's coordination number in a PIMD simulation of D_2O adsorption at 300 K with 16 beads, where no D_2O dissociation is observed, highlighting the pronounced kinetic isotope effect. Figure S8 displays the time evolution of the mean square displacements predicted by MTP for the dissociated H atoms, the H and O atoms within the intact or dissociated water overlayers. Figure S9 zooms in on Fig. 2(b) from the main text, but focuses on the time period surrounding the first dissociation event. Figure S10 is similar to Fig. S9, but focuses on the time period surrounding the second dissociation event. Figure S11 is similar to Fig. S9, but focuses on the time period surrounding the third dissociation event.

We emphasize that the predictions derived from our MLP are both accurate and robust. This reliability stems from the generation of our MLP using a highly descriptive training dataset that comprehensively spans the relevant phase space. To validate this, we computed the extrapolation grade for centroid structures obtained by averaging all beads from the long-timescale PIMD trajectories corresponding to Fig. 2(b) in the main text. As illustrated in Fig. S12(a), all centroid structures exhibit an extrapolation grade below 1.3, confirming that our MLP operates within the interpolation regime [25]. This result underscores the reliability of our MLP-derived conclusions. To further validate the MLP, we randomly selected 100 centroid structures from the PIMD trajectories, encompassing both intact and dissociated water configurations. We compared the energies and forces predicted by the MLP with those computed using DFT. As demonstrated in Figs. S12(b) and (c), the MLP predictions show excellent agreement with the DFT results, reinforcing the accuracy and reliability of our MLP-accelerated PIMD predictions.

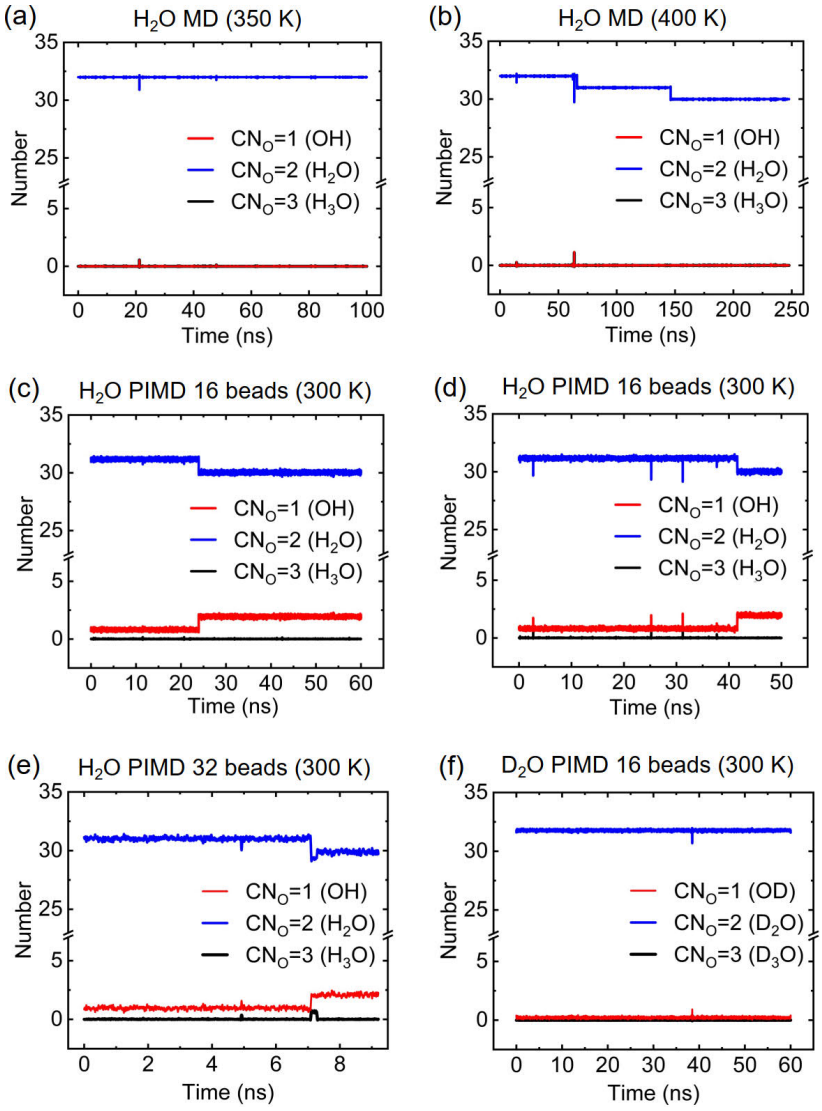

Figure S7. Time evolution of the number of OH (CN_O=1), H_2O (CN_O=2), and H_3O (CN_O=3) species in (a) a classical MD simulation at 350 K, (b) a classical MD simulation at 400 K, and (c)-(d) two independent PIMD simulations at 300 K with 16 beads. CN_O represents the coordination number of the oxygen atom. Note that the reduction of H_2O in panel (b) is due to the evaporation of water at 400 K into the vacuum. However, even at this high temperature, no dissociation of water is observed. (e) Time evolution of the oxygen atom's coordination number in a PIMD simulation of H_2O adsorption at 300 K with 32 beads. (f) Time evolution of the oxygen atom's coordination number in a PIMD simulation of D_2O adsorption at 300 K with 16 beads. Here, all simulations employed the same initial supercell structure as used in Fig. 2 of the main text.

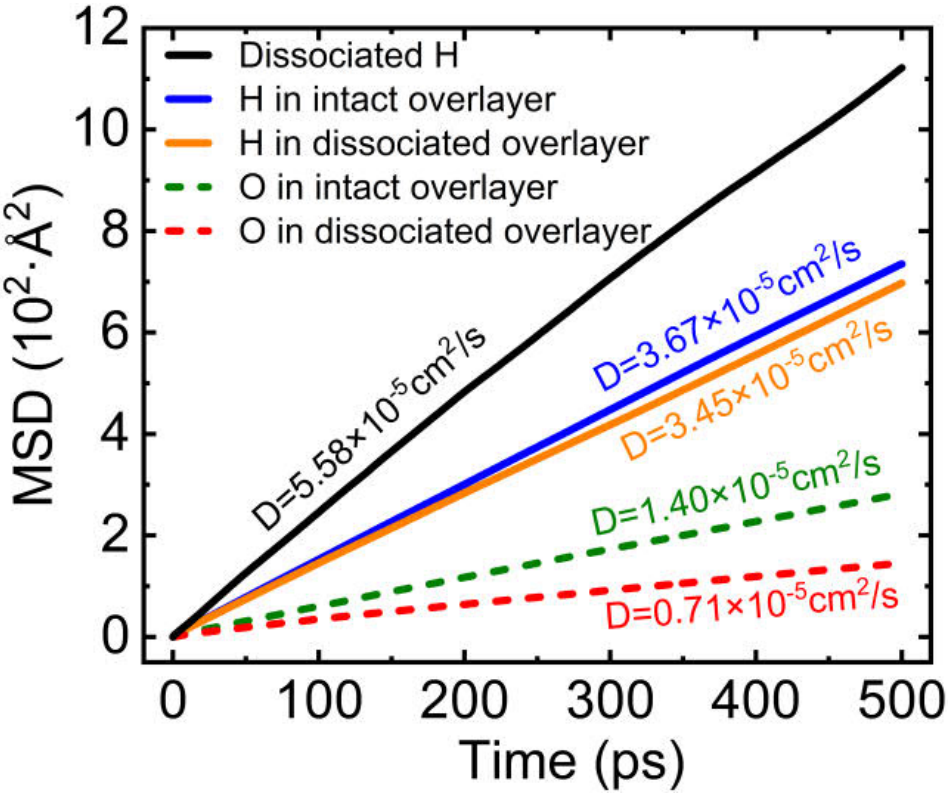

Figure S8. Time evolution of the mean square displacements (MSD) for dissociated H atoms, as well as H and O atoms within intact or dissociated water overlayers predicted by the PIMD simulations at 300 K. The diffusion coefficients are indicated as calculated using the formula $D = \frac{1}{4}\frac{dMSD}{dt}$ where t represents the time.

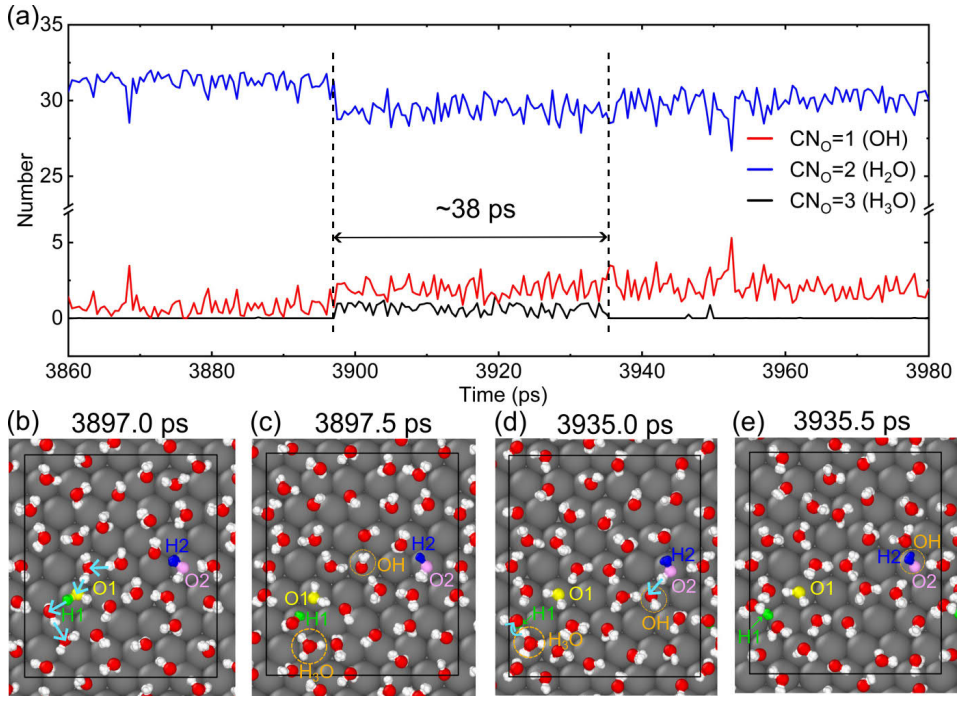

Figure S9. (a) Time evolution of the number of OH (CN_O=1), H_2O (CN_O=2), and H_3O (CN_O=3) species in the same PIMD simulation as in Fig. 2(b) of the main text, but with a focus on the time period surrounding the first dissociation event. CN_O represents the coordination number of the oxygen atom. The estimated lifetime of the H_3O species is indicated. (b)-(e) Snapshots from the PIMD trajectory. The tracked O and H atoms as well as the H_3O and OH species are highlighted. The cyan arrows depict the proton transfer process.

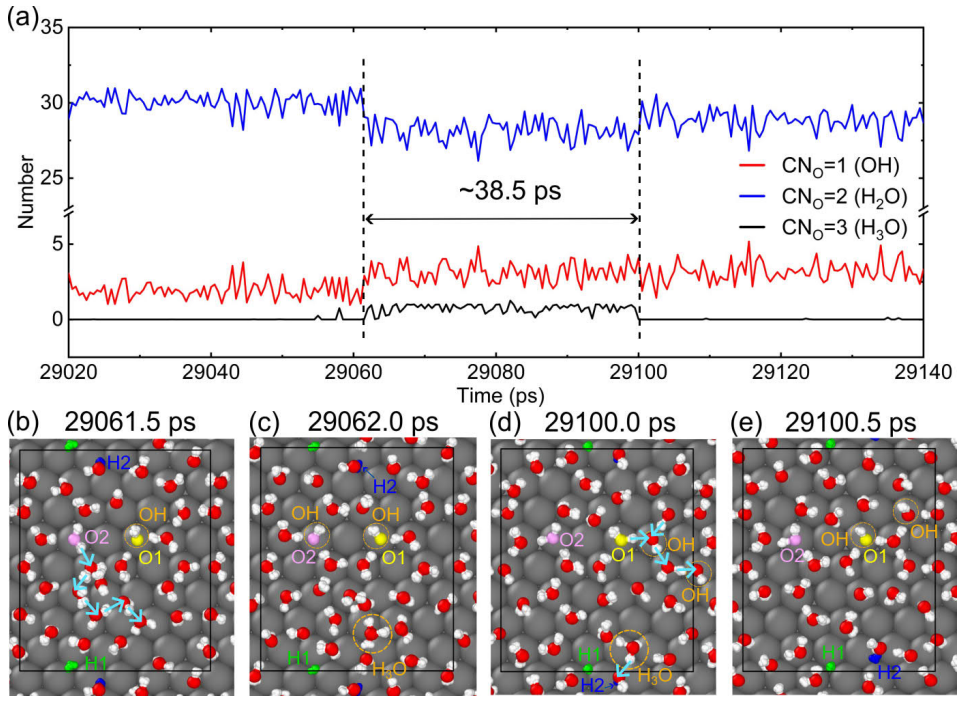

Figure S10. Same as Fig. S9, but with a focus on the time period surrounding the second dissociation event.

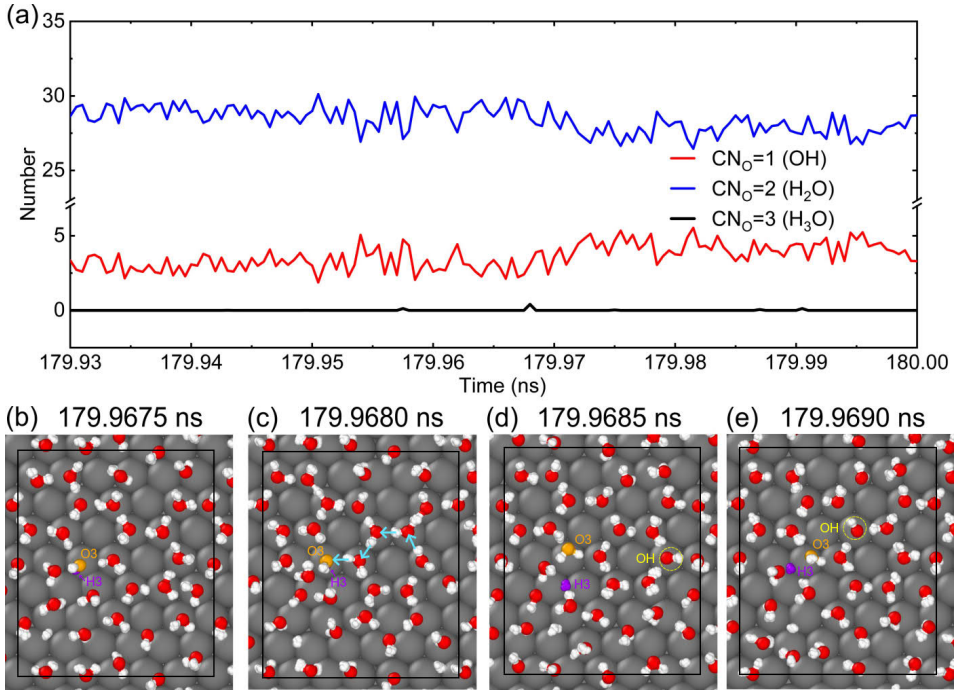

Figure S11. Same as Fig. S9, but with a focus on the time period surrounding the third dissociation event.

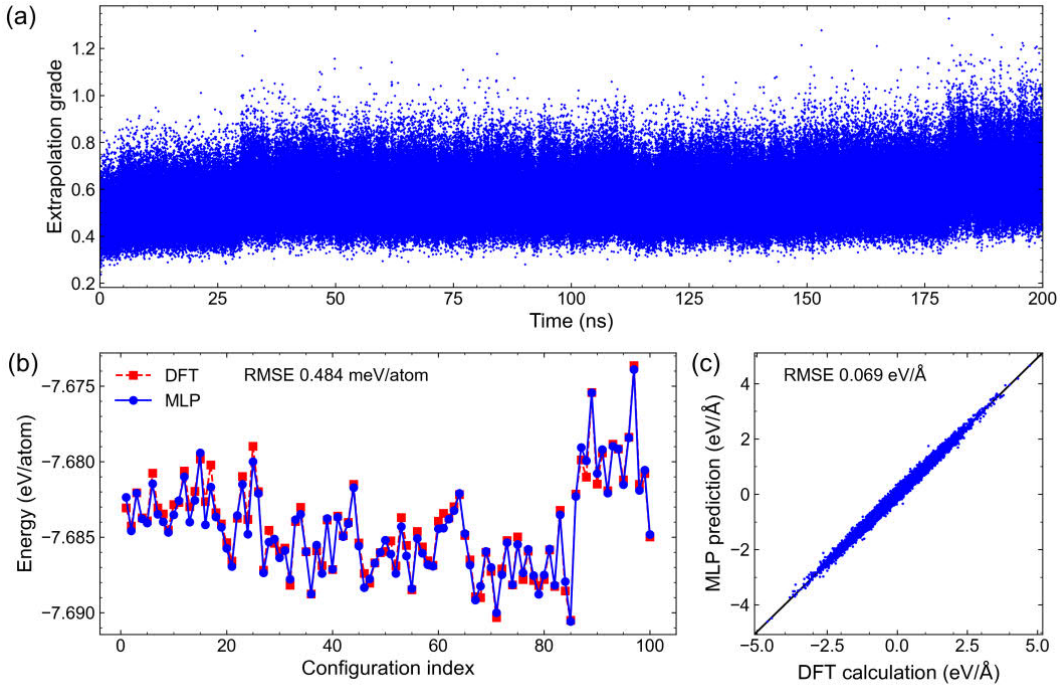

Figure S12. (a) Time evolution of the extrapolation grade for all centroid structures obtained by averaging all beads in the 200-nanosecond PIMD simulations (corresponding to the case in Fig. 2(b) of the main text). (b) Comparison of energies predicted by MLP and DFT for 100 randomly selected centroid structures. (c) MLP-predicted forces versus DFT results for the same 100 centroid structures. The root-mean-square errors (RMSEs) for energies and forces are also provided for quantitative assessment.

VIII. DATA AVAILABILITY

The data supporting the findings of this study, such as the training and validation datasets, the developed MTP, and the initial and final structures as well as the LAMMPS input scripts for both MD and PIMD simulations, are publicly available at https://github.com/wftao1995/Water-Dissociation-on-Ru-0001-Dataset.

[1] G. Kresse and J. Hafner, "Ab initio molecular dynamics for liquid metals," Phys. Rev. B **47**, 558–561 (1993).
[2] G. Kresse and J. Furthmüller, "Efficient iterative schemes for ab initio total-energy calculations using a plane-wave basis set," Phys. Rev. B **54**, 11169–11186 (1996).
[3] B. Hammer, L. B. Hansen, and J. K. Nørskov, "Improved adsorption energetics within density-functional theory using revised perdew-burke-ernzerhof functionals," Phys. Rev. B **59**, 7413–7421 (1999).
[4] P. E. Blöchl, "Projector augmented-wave method," Phys. Rev. B **50**, 17953–17979 (1994).
[5] G. Kresse and D. Joubert, "From ultrasoft pseudopotentials to the projector augmented-wave method," Phys. Rev. B **59**, 1758–1775 (1999).
[6] Stefan Grimme, Jens Antony, Stephan Ehrlich, and Helge Krieg, "A consistent and accurate ab initio parametrization of density functional dispersion correction (DFT-D) for the 94 elements H-Pu," The Journal of Chemical Physics **132**, 154104 (2010).
[7] Jonas Weissenrieder, Anders Mikkelsen, Jesper N. Andersen, Peter J. Feibelman, and Georg Held, "Experimental evidence for a partially dissociated water bilayer on Ru(0001)," Phys. Rev. Lett. **93**, 196102 (2004).
[8] Mark Gallagher, Ahmed Omer, George R Darling, and Andrew Hodgson, "Order and disorder in the wetting layer on Ru(0001)," Faraday Discussions **141**, 231–249 (2009).
[9] John P. Perdew, Kieron Burke, and Matthias Ernzerhof, "Generalized gradient approximation made simple," Phys. Rev. Lett. **77**, 3865–3868 (1996).
[10] Jiří Klimeš, David R Bowler, and Angelos Michaelides, "Chemical accuracy for the van der waals density functional," Journal of Physics: Condensed Matter **22**, 022201 (2009).
[11] Jianwei Sun, Adrienn Ruzsinszky, and John P. Perdew, "Strongly constrained and appropriately normed semilocal density functional," Phys. Rev. Lett. **115**, 036402 (2015).
[12] Katrin Forster-Tonigold and Axel Groß, "Dispersion corrected RPBE studies of liquid water," The Journal of Chemical Physics **141**, 064501 (2014).
[13] Tobias Morawietz, Andreas Singraber, Christoph Dellago, and Jörg Behler, "How van der waals interactions determine the unique properties of water," Proceedings of the National Academy of Sciences **113**, 8368–8373 (2016).
[14] John W. Arblaster, "Crystallographic properties of ruthenium," Platinum Metals Review **57**, 127–136 (2013).
[15] Peter J. Feibelman, "Lattice match in density functional calculations: ice Ih vs. β-AgI," Phys. Chem. Chem. Phys. **10**, 4688–4691 (2008).
[16] Peter J Feibelman, "Partial dissociation of water on Ru (0001)," Science **295**, 99–102 (2002).
[17] Javier Carrasco, Biswajit Santra, Ji ří Klimeš, and Angelos Michaelides, "To wet or not to wet? dispersion forces tip the balance for water ice on metals," Phys. Rev. Lett. **106**, 026101 (2011).
[18] M. Tatarkhanov, E. Fomin, M. Salmeron, K. Andersson, H. Ogasawara, L. G. M. Pettersson, A. Nilsson, and J. I. Cerdá, "The structure of mixed H_2O-OH monolayer films on Ru(0001)," The Journal of Chemical Physics **129**, 154109 (2008).
[19] Martin Schilling and R. Jürgen Behm, "Partial dissociation of water on Ru(0001) at low temperatures–adsorption, structure formation and hydrogen passivation effects," Surface Science **674**, 32–39 (2018).
[20] Di Zhao, Feng Liu, Xiangmei Duan, and Deyan Sun, "Intrinsic disorder of dangling OH-bonds in the first water layer on noble metal surfaces," Computational Materials Science **201**, 110863 (2022).
[21] Peitao Liu, Jiantao Wang, Noah Avargues, Carla Verdi, Andreas Singraber, Ferenc Karsai, Xing-Qiu Chen, and Georg Kresse, "Combining machine learning and many-body calculations: coverage-dependent adsorption of CO on Rh(111)," Physical Review Letters **130**, 078001 (2023).
[22] Mingfeng Liu, Jiantao Wang, Junwei Hu, Peitao Liu, Haiyang Niu, Xuexi Yan, Jiangxu Li, Haile Yan, Bo Yang, Yan Sun, Chunlin Chen, Georg Kresse, Liang Zuo, and Xing-Qiu Chen, "Layer-by-layer phase transformation in Ti_3O_5 revealed by machine-learning molecular dynamics simulations," Nature Communications **15**, 3079 (2024).
[23] Ryosuke Jinnouchi, Jonathan Lahnsteiner, Ferenc Karsai, Georg Kresse, and Menno Bokdam, "Phase transitions of hybrid perovskites simulated by machine-learning force fields trained on the fly with bayesian inference," Physical Review Letters **122**, 225701 (2019).
[24] Ryosuke Jinnouchi, Ferenc Karsai, and Georg Kresse, "On-the-fly machine learning force field generation: application to melting points," Physical Review B **100**, 014105 (2019).
[25] Ivan S Novikov, Konstantin Gubaev, Evgeny V Podryabinkin, and Alexander V Shapeev, "The MLIP package: moment tensor potentials with MPI and active learning," Machine Learning: Science and Technology **2**, 025002 (2021).
[26] Jiantao Wang, Peitao Liu, Heyu Zhu, Mingfeng Liu, Hui Ma, Yun Chen, Yan Sun, and Xing-Qiu Chen, "Efficient moment tensor machine-learning interatomic potential for accurate description of defects in ni-al alloys," arXiv:2411.01282 (2024).
[27] Graeme A Henkelman, Blas Pedro Uberuaga, and Hannes Jónsson, "A climbing image nudged elastic band method for finding saddle points and minimum energy paths," Journal of Chemical Physics **113**, 9901–9904 (2000).
[28] Aidan P. Thompson, H. Metin Aktulga, Richard Berger, Dan S. Bolintineanu, W. Michael Brown, Paul S. Crozier, Pieter J. in 't Veld, Axel Kohlmeyer, Stan G. Moore, Trung Dac Nguyen, Ray Shan, Mark J. Stevens, Julien Tranchida, Christian Trott, and Steven J. Plimpton, "Lammps-a flexible simulation tool for particle-based materials modeling at the atomic, meso, and continuum scales," Computer Physics

Communications **271**, 108171 (2022).
[29] Nosé Shuichi, "Constant temperature molecular dynamics methods," Progress of Theoretical Physics Supplement **103**, 1–46 (1991).